Natural Crack Diagnosis System Based on Novel L-Shaped Electromagnetic Sensing Thermography

Zewei Liu, Bin Gao, *Senior Member, IEEE*, and Gui Yun Tian, *Senior Member, IEEE*

***Abstract*—Nondestructive detection of small fatigue cracks is a critical and challenging task in evaluating the properties of material. This article proposes a novel L-shaped ferrite magnetic open sensing structure of the eddy current pulsed thermography system for fatigue crack inspection on metallic materials with anomalistic geometry. The theoretical derivation model of the proposed structure is developed to generate a guided distribution of electromagnetic field for enhancing the weak thermal signal detection. The proposed detection model provides a region of interest that has relatively uniform magnetic field. This significantly enhances the detectability and thermal contrast of omnidirectional microfatigue cracks. In addition, the detection is completely in the open view of the infrared camera, and the configuration has advantages of dramatically increasing portability and efficiency for detecting complex workpiece. Experiments on natural cracks in several samples have been conducted to validate the reliability and efficiency of the proposed system.**

***Index Terms*—Complex workpiece, electromagnetic field, fatigue crack detection, induction thermography.**

I. Introduction

IN MANY industrial branches, especially in the production of critical components and elements, the safety and reliability of applied metal components are of extreme importance [1], [2]. Nondestructive evaluation (NDE) [3], [4] is a typical effective sensing approach to monitor and diagnose material characteristics and structural degradation without destroying the serviceability of a component.

Manuscript received March 22, 2019; revised June 14, 2019 and October 15, 2019; accepted October 27, 2019. Date of publication November 15, 2019; date of current version July 14, 2020. The work was supported in part by National Natural Science Foundation of China under Grant 61971093, Grant 61527803, and Grant 61960206010, in part by the Science and Technology Department of Sichuan, China, under Grant 2019YJ0208, Grant 2018JY0655, and Grant 2018GZ0047, and in part by the Fundamental Research Funds for the Central Universities under Grant ZYGX2019J067. *(Corresponding author: Bin Gao.)*

Z. Liu and B. Gao are with the School of Automation Engineering, University of Electronic Science and Technology of China, Chengdu 611731, China (e-mail: 1433427550@qq.com; bin_gao@uestc.edu.cn).

G. Y. Tian is with the School of Automation Engineering, University of Electronic Science and Technology of China, Chengdu 611731, China, and also with the School of Engineering, Newcastle University, NE1 7RU Newcastle upon Tyne, U.K. (e-mail: g.y.tian@ncl.ac.uk).

Color versions of one or more of the figures in this article are available online at http://ieeexplore.ieee.org.

Digital Object Identifier 10.1109/TIE.2019.2952782

The most widely used NDE methods for fatigue crack detection are magnetic particle testing (MT), penetrant testing (PT), ray testing (RT), and eddy current testing (ECT) [5], [6]. MT is effective in detecting surface and near surface discontinuities. However, the procedure of MT is complicated, and the surface of the sample requires pretreatment [4], [6]. PT is a low-cost inspection method, and it is sensitive to an opening surface crack. Unfortunately, the inspection should be on a smooth clean surface, and it produces pollution [7]. RT can obtain intuitive results, whereas the radiation is a potential safety problem. The sensing techniques based on the electromagnetic field [1], [8], i.e., ECT [9], magnetic flux leakage (MFL), and alternating current field measurement (ACFM) [10], have a unique advantage in NDE since the electromagnetic properties are easily influenced by the vary of microstructure parameters. In addition, they are sensitive to load-induced and residual stress. ECT is the most widely applied detection method out of all electromagnetic NDE techniques [11], [12]. Since the probe does not have to contact the work surface, ECT is useful for near surface with wet films or coatings. Nevertheless, the testing result of ECT is highly influenced by lift-off variation.

As an attractive technique, infrared thermography (IRT) has gained popularity in NDE applications [13], [14]. The outstanding advantage of IRT can be drawn that it can perform a rapid inspection over a large area with high spatial resolution and sensitivity within a short period. In addition, IRT technique matches the demands of automotive production with its high cycle times and fully automated process.

Eddy current pulsed thermography (ECPT) [15], [16] is a multiphysical coupling NDE technique for conductive material, which combines the well-established inspection techniques of eddy current, magnetism, and IRT. The material properties, such as electrical conductivity, magnetic permeability, and thermal conductivity, are used by ECPT to identify and evaluate the characteristic of defects. In particular, material variation, structural stress, and fatigue or damages are efficiently recorded and demonstrated through thermal image sequences, and these can be evaluated by Joule heating via eddy current, heat conduction, and IRT.

The configuration of ECPT determines the distribution of magnetic field and electric field around the workpiece, thereby affecting results from the induction sensing system [17]. The signal-to-noise ratio (SNR) and detection sensitivity of ECPT

depend on the intensity and uniformity of the excitation. Consequently, there are several studies focusing on optimizing the parameters of excitation, modifying the excitation structure, and adjusting the position of the inductor [18]. Tsopelas *et al.* [19] investigated the effect of the angle of inclination of the exciting coil and found the factors in determining the uniformity of temperature field by varying the lift-off distance as well as cross-sectional area of the coil. He *et al.* [20] proposed a ferrite-yoke inductor to obtain an open field imaging to study the characteristics and mechanism of the defect detection. Gao *et al.* [21] combined MFL and ECPT to detect rail surface cracks. Goldammer *et al.* [22] applied triangular-shaped coil for an automated detection system, which is acceptable for both moving and stationary inspection. Tian *et al.* [23] used a rectangular single-turn coil to evaluate the contact damage of gear and compared the performance of square planar inductor with circular inductor. Oswald-Tranta [24] inserted the sample into a helix coil to detect surface crack of the material. Hansen *et al.* [25] proposed an asymmetric inductor to achieve the uniform heating. Peng *et al.* [26] investigated Helmholtz-coil-based ECPT system to detect RCF cracks. However, the issues of poor applicability to different specimens, limited detection area, and low detection sensitivity in ECPT are still challenging for defect characterization. In addition, the proximity and geometry effect of the test samples have significant impact on the current density distribution in conductors as this leads to remaining detection problems to inspect the small natural cracks [27], [28]. In particular, multiple cracks, such as rolling contact fatigue (RCF) cracks, and defects occurring in the weld part as well as screw joints are of great importance since they can constitute a starting point for serious damages.

This article establishes a new L-shaped ferrite magnetic open excitation structure of electromagnetic–thermal ECPT model to enhance the detectability of microfatigue cracks in metallic materials with anomalistic shape. In this model, most of magnetic force lines are concentrated in the region of interest (ROI), where the electromagnetic field is approximately to be uniform. Thus, the sensitivity of detection can be significantly enhanced. In addition, the ROI is completely in the open view of the infrared camera, and it provides a possibility of dramatically increasing portability and efficiency for detecting the in-service workpiece. The detection capability of the proposed method has been demonstrated through both simulation and real experiments.

The rest of this article has been organized as follows. Section II describes the theoretical model of the new configuration of ECPT. Section III implements the simulation and experiment studies. Finally, Section IV concludes this article.

II. Methodology

A. ECPT System and the New Excitation Configuration

The new configuration of ECPT system is proposed and illustrated in Fig. 1. Specifically, the excitation structure is made of open-view ferrite core and copper helix coil. At the same time, the infrared camera is positioned normal to the surface of the conductive material. The proposed configuration is a hybrid of magnetic flux, eddy current, and thermography, which

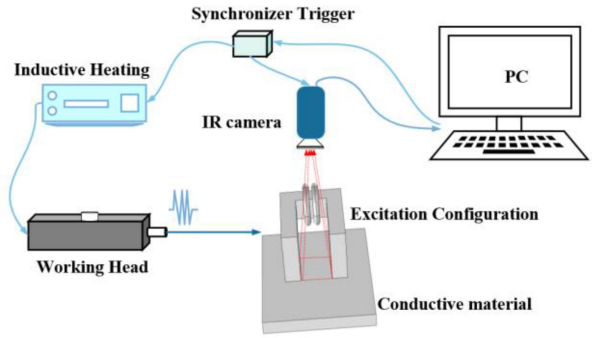

Fig. 1. New configuration of ECPT system.

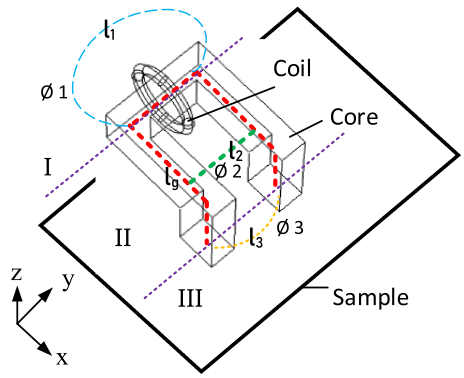

Fig. 2. Magnetic flux path of the structure.

combines the advantages of multiple physical effects and makes the detection more efficient.

When the control device generates a signal to activate the system, high-frequency pulsed current flows through the helix coil and generates alternating magnetic field. The ferrite core collects the magnetic flux, and the flux is transmitted to the sample between the two poles of core through a magnetic circuit. These include ferrite core, the air gap, and the sample. If defect exists in the conductive material, the distribution of magnetic field, the eddy current intensity, and the process of thermal diffusion will be affected. Consequently, the transient time–spatial characteristics of radiative heat transfer modes over the plate surface can be captured by an infrared camera.

B. Mathematical Models of Magnetic Flux and Eddy Current

In this article, the sample under inspection has the shape of thin plate and lines in the x–y plane. Fig. 2 shows the magnetic flux path schematic diagram. The magnetic flux generated by the L-shaped structure in the space can be divided into three parts. Part I denotes the flux flow through the air. One of the magnetic flux paths in this part is represented as the blue dotted circle, and the average length of the paths in the part I is l_1. Part II denotes the flux flow through the L-shaped core and the air between the two poles of the core. The flux flow through the magnetic core is marked with the red dotted line, and one of the flux paths in the air is marked with the green dotted line. The distance between

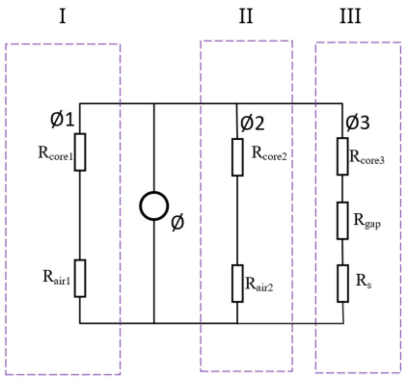

Fig. 3. Magnetic circuit model of the structure.

the two poles of the core is l_2. Part III denotes the flux flow through the core and the sample that is placed directly below the L-shaped core. The flux flow through L-shaped core is marked with the red dotted line with the average length of l_g, one of the flux paths below the core is represented as the yellow dotted line with the average length of l_3. In addition, the magnetic flux below the sample can be neglected.

The magnetic circuit model of the proposed structure is shown in Fig. 3. $\emptyset$ is the magnetic flux that is generated by the coil with high-frequency electric current. The magnetic flux in parts I, II, and III is $\emptyset 1$, $\emptyset 2$, and $\emptyset 3$, respectively. According to the magnetic circuit theory [29], the magnetic flux distribution can be derived. The relationship between magnetic flux and the reluctance of the magnetic circuit is given as follows:

$$\text{mmf} = NI = \emptyset R \tag{1}$$

where $\emptyset$ is magnetic flux, R is reluctance of a magnetic circuit, mmf denotes magnetic motive force, and it is produced by the current I of the coil with N turns.

The reluctance in the parts I, II and III is represented as R_1, R_2, and R_3, respectively. According to the calculation formula of the reluctance, R_1, R_2, and R_3 can be given as follows:

$$R_1 = R_{\text{core1}} + R_{\text{air1}} = \frac{l_1}{\mu_0 A_{r1}} + \frac{l_2}{\mu_c A_c} \tag{2}$$

$$R_2 = R_{\text{core2}} + R_{\text{air2}} = \frac{l_2}{\mu_0 A_{r2}} + \frac{l_x}{\mu_c A_c} \tag{3}$$

$$\begin{aligned} R_3 &= R_{\text{core3}} + R_{\text{gap}} + R_s \\ &= \frac{l_g}{\mu_c A_c} + \frac{l_{\text{gap}}}{\mu_0 A_{\text{gap}}} + \frac{l_s}{\mu_s A_s} \end{aligned} \tag{4}$$

where μ_0, μ_c, and μ_s are the permeability of air, core, and sample, respectively. A_{r1}, A_{r2}, A_{gap}, A_c, and A_s are the cross area in the flux path of the air in the part I, the air in part II, the air in part III, the core, and the sample, respectively.

In the model, the permeability of the core $\mu_c \gg \mu_s$ and $\mu_c \gg \mu_0$. For ferromagnetic simple, $\mu_s \gg \mu_0$, and for the nonferromagnetic simple, $\mu_s = \mu_0$. It can be assumed that the reluctance of ferrite core is $R_{\text{core1}} = R_{\text{core2}} = R_{\text{core3}} = 0$ due to its high permeability.

1) For ferromagnetic material, $R_{\text{gap}} = 0$, $R_3 \ll R_1$, $R_3 \ll R_2$, and $R_s \gg R_{\text{core3}}$. Thus, the flux flow through the sample is far more than that of the other parts.
2) For nonferromagnetic material, $R_{\text{gap}} = 0$. A_{r2} is the cross area of the air between magnetic core in the flux path, the magnetic flux flow through the part II is large. Thus, for nonferromagnetic material, the flux flow through both the nonferromagnetic sample and the air between the magnetic poles. Since l_s approximates to l_2, the magnetic flux density in the sample is on the same order of magnitude as that of the air between the magnetic poles.
3) When there is a gap between the core and the sample of ferromagnetic material: $R_{\text{gap}} > 0$. As the length of the gap (lift-off distance) increases, the reluctance of the magnetic circuit increase. When $l_{\text{gap}} < l_2$, the attenuation of magnetic field is related to the l_{gap}. When $l_{\text{gap}} > l_2$, little flux passes through the specimen. In the numerical simulation experiment, different lift-off distances have been conducted to validate the influence for defect detection.
4) When there is a gap between the core and the sample of nonferromagnetic material, $R_{\text{gap}} > 0$. $R_3 > R_2$, and $R_3 > R_1$. There will be a great decline of the magnetic flux density in the sample when the length of the gap increases.

From abovementioned analysis, it can be concluded that the distribution of the magnetic flux is influenced by the material of the sample, the size of the magnetic core, and the relative position. The L-shaped magnetic yoke guided part of the magnetic flux into the sample. In this model, leakage flux will not affect the distribution of eddy current induced in the conductive material, and flux in the ROI of the sample is highlighted.

The electromagnetic fields in the sample are governed by differential Maxwell's equations [30]

$$\nabla \times H = J_e + J_s + \frac{\partial D}{\partial t} \tag{5}$$

$$\nabla \times E = -\frac{\partial B}{\partial t} \tag{6}$$

where H is magnetic field intensity, J_e is the induced current density, J_s is the external current density, D is the electric displacement vector, and E is the electric field intensity.

The constitutive equations for the electromagnetism are define as follows:

$$D = \varepsilon E \tag{7}$$

$$J_e = \sigma E \tag{8}$$

$$B = \mu H \tag{9}$$

where B is the magnetic flux density, ε is the permittivity of the medium, σ is the electrical conductivity, and μ is the permeability.

Defining a magnetic vector potential A in the (x, y) plane is given by

$$\text{B} = \nabla \times \text{A}. \tag{10}$$

The electromagnetic governing equation can be written as

$$\nabla \times \left(\frac{1}{u}\nabla \times \mathrm{A}\right) + \sigma\frac{\partial A}{\partial t} + \varepsilon\frac{\partial^2 A}{\partial t^2} = J_s. \tag{11}$$

The induction of electromagnetic field is related to the conductivity and permeability of the material, which influences both direction and property of propagation. Therefore, the boundary from different materials is utilized to depict better constraint conditions when electromagnetic field propagates into the different mediums. Denoting the conducting region by "c" and the air (external) region by "a," the boundary conditions on the boundary surface S takes the following form:

$$E_{tc|S} = E_{ta|S} \tag{12}$$

$$H_{tc|S} - H_{ta|S} = J_s \tag{13}$$

where the subscripts t and n indicate tangential and normal directions, respectively. Thus, the tangential component of the magnetic field is discontinuous.

The vector potential in the air region satisfies the Laplace equation

$$\nabla^2 A_a = 0. \tag{14}$$

For the flat parallel field, the boundary conditions are obtained in the following forms:

$$A_{c|S} = A_{a|S} \tag{15}$$

$$\left.\frac{\partial A_c}{\partial n}\right|_S = \left.\frac{\partial A_a}{\partial n}\right|_S. \tag{16}$$

For the defect detection in electromagnetic thermography, the high-frequency magnetic flux is used to induce eddy current and generate heat in the sample. Thus, the frequency has a great impact on the induction heating when the amplitude of the magnetic flux density is limited within a range. The excitation frequency in this model is typically chosen as several hundred kilohertz to generate intense eddy current in the sample. The displacement current density at this frequency is negligible. After setting the above-mentioned boundary conditions on the surface of the conductor, the distribution of electromagnetic field can be solved using the finite-element method.

The expulsion of electromagnetic field from the sample occurs as described by Lenz's law, and the electromagnetic skin depth δ is given as follows:

$$\delta = \frac{1}{\sqrt{f\pi\mu\sigma}} \tag{17}$$

where f is the frequency of the pulsed current.

The distribution of magnetic field on the specimen is illustrated in Fig. 4. The area outlined within blue marked line is the ROI in which the magnetic field is relatively uniform. This is extremely advantageous for detecting defects on the surface of the conductor.

When a defect exists in the ROI, the uniform eddy current will be destroyed. Specifically, the highest current density will be concentrated in tips and bottom of the notch.

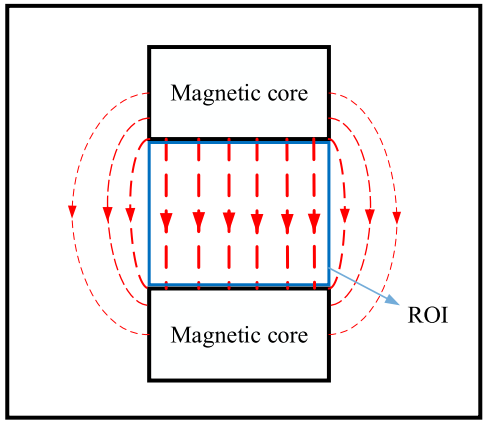

Fig. 4. Magnetic field distribution and the ROI.

C. Thermal Field Analysis

As a resistance exists in metal materials, the eddy current enables the conductor to generate heat. The Joule heat bridges the thermal field and eddy current field. This relationship between the generated heat Q and electric field intensity vector E can be expressed as

$$Q = \frac{1}{\sigma}|J_e|^2 = \frac{1}{\sigma}|\sigma E|^2. \tag{18}$$

By taking account of Joule heating and heat diffusion, the temperature distribution can be calculated as

$$\frac{\partial T}{\partial t} = \frac{K}{\rho C_p}\left(\frac{\partial^2 T}{\partial x^2} + \frac{\partial^2 T}{\partial y^2} + \frac{\partial^2 T}{\partial z^2}\right) + \frac{1}{\rho C_p} q\,(x, y, z, t) \tag{19}$$

where $T = T(x, y, z, t)$ denotes the temperature distribution, K denotes the thermal conductivity of the material, ρ denotes the density, C_p denotes the specific heat capacity, and $q(x, y, z, t)$ denotes the generated internal heat per unit volume and unit time, which is the result of the Joule heating by eddy current.

From the formula of the temperature distribution, the generated Joule heat will conduct from the high temperature point to low temperature point. When there exists a defect in the ROI, horizontal thermal conduction will be blocked in the defect edge due to the sudden decrease in the heat transfer. At the same time, the temperature is conducting from the surface of the specimen to the subsurface, which is termed longitudinal thermal conduction. Consequently, part of the heat accumulates in the defect edge or bottom in the cooling stage. In the proposed structure, this characteristic can be extracted to detect omnidirectional defects for a relatively uniform electromagnetic field that can be generated within the ROI.

D. Infrared Radiation Analysis

Due to the constant motion of charged particles inside any object, when the temperature of the object is above the absolute zero, it will continuously absorb or emit electromagnetic radiation, mainly infrared radiation. The radiant intensity I is the radiant power that is emitted from a point source of a radiating

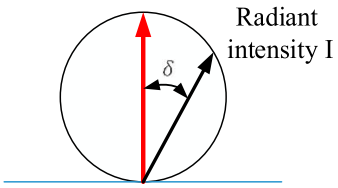

Fig. 5. Radiant intensity depends on the direction of emission.

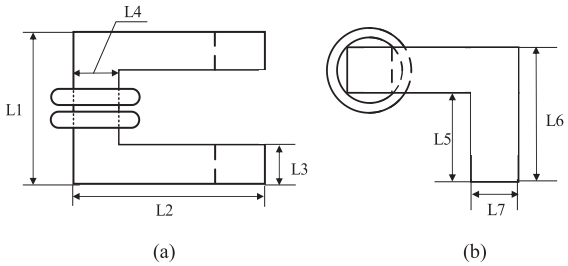

Fig. 6. (a) Vertical view and (b) side view of the coil with core.

TABLE I
DIMENSIONS OF THE EXCITATION CONFIGURATION

Parameters	L1	L2	L3	L4	L5	L6	L7
Values(mm)	40	50	10	15	20	35	15

object into a solid angle element in the given direction

$$I = I_0 \cdot \cos\delta \tag{20}$$

where I_0 is radiation intensity in the normal direction of the surface, δ is the angle between the observed direction and surface normal.

The angular dependence of radiant intensity is schematically depicted in Fig. 5. Thus, the radiant intensity is observed to be the largest when the direction is perpendicular to the surface. The proposed open view model enables the radiance detected by IR camera to be maximal.

III. Experiment Setup

A. Numerical Experiment and Results

In order to validate the electromagnetic characteristics of the detection mechanism, several finite-element simulation models are established. All simulation experiments for crack detection on both a plate and a complex geometric structure surface are implemented by the inductive heating module of the COMSOL Multiphysics platform.

The schematic of views of the simulation model are shown in Fig. 6. Specifically, the helix coil is made of copper, and the magnetic core is made of ferrite. The dimensions of the configuration for simulation model are shown in Table I. The radius and wire diameter of the helix coil with two turns are 12.7 and 4 mm, respectively. In these simulation experiments, the magnitude of the current flowing through the coil is 350 A,

TABLE II
MATERIAL PARAMETERS

Parameters	copper	ferrite	316#	45#
Conductivity (S/m)	5.998e7	1e-6	1.3e6	5.5e6
Relative permeability	1	2000	1	190
Density (kg/m3)	8700	7800	7990	7850
Heat capacity (J/(kg K))	385	600	502	475
Thermal conductivity (W/(m K))	400	5	12.1	51.9

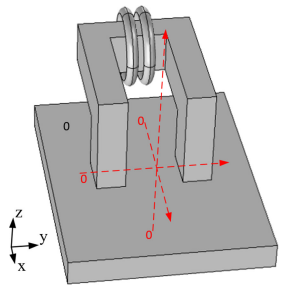

Fig. 7. Space diagram and the direction of *x, y, z*.

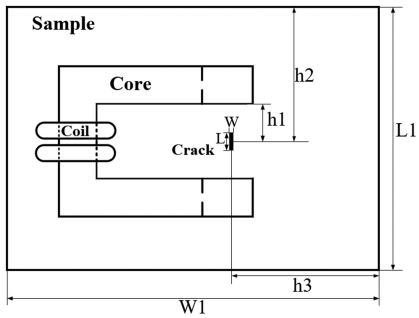

Fig. 8. Top view of the detection model.

the frequency is 200 kHz, and the initial temperature value is 293.15 k.

The distribution of electromagnetic field in the ROI of nondefective plate sample has been researched. The detection performance of variety orientation cracks and different lift-off distances in both ferromagnetic and nonferromagnetic samples has been validated. In addition, the detection for the sample with a complex geometry has been carried out. In the experiments, 45# steel is ferromagnetic, and 316# stainless steel is nonferromagnetic. The setting of physical parameters, including conductivity, relative permeability, density, heat capacity, and thermal conductivity, of the materials is shown in Table II. Note that the change of permeability caused by heating can be neglected as the temperature is far less than Curie temperature.

1) Numerical Simulation Experiment for the Distribution of Electromagnetic Field in the ROI: The space diagram of the model with direction *x, y, z* and the position of coordinate axis line are shown in Fig. 7. A nondefective metal plate sample with 6 mm thickness, 100 mm length, and 80 mm width is employed for the experiment. Fig. 8(a) shows the distribution of magnetic

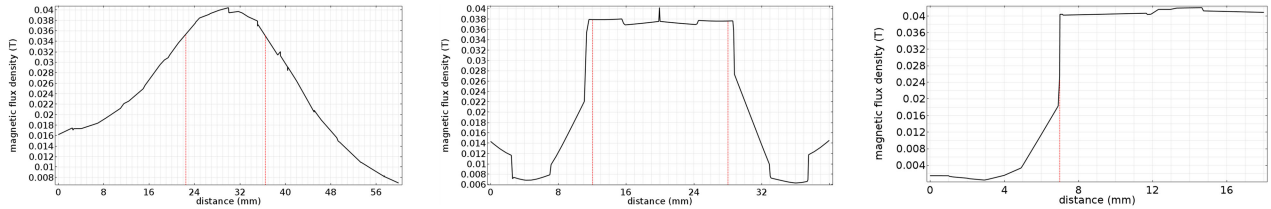

Fig. 9. Distribution of magnetic flux density (a) under different *x* distance, (b) under different *y* distance, and (c) under different *z* distance.

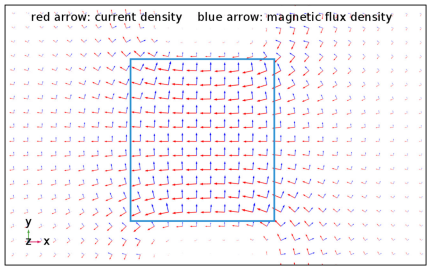

Fig. 10. Magnetic flux vectors and induced current vectors without defect.

flux density on the surface under different x distance, and the length of the ROI in the x-direction is marked with red dotted line. Fig. 8(b) shows the distribution of magnetic flux density on the surface under different y distance, and the length of the ROI in the y-direction is marked with red dotted line. Fig. 8(c) shows the distribution of magnetic flux density on the surface under different z distance. The point of distance 7 mm is the surface of the sample, which is marked with red dotted line. From Fig. 8(a), the magnetic flux density in the ROI is greater than that of the other regions with the variation of 12.5%. As can be seen in Fig. 8(b), the maximum variation of the magnetic flux density in the y-direction of the ROI is 7.6%. As can be seen from Fig. 8(c), the magnetic flux density decreases greatly below the surface of the sample. Thus, the magnetic flux is concentrated on the sample surface. In addition, the magnetic flux density on the surface is equals to that of the air between the magnetic poles directly above the sample. Fig. 9 shows the calculate result of magnetic field and electric field distribution on the plate surface without defect. The magnitude and the direction of the field is represented by the arrow. It can be concluded that a relatively uniform electromagnetic field is induced in the ROI.

2) Defect Detection of Plate: Fig. 10 shows the top view of the detection model, and it shows the relative position between the magnetic core and the specimen. The width and length of the crack are marked as W and L, respectively. The size of the fatigue natural cracks is small, and it is set as $L \times W \times D = 3$ mm $\times$ 0.3 mm $\times$ 1 mm in this simulation. To validate the detection ability of variety orientation cracks, four different angles (α) are designed, which are 0°, 30°, 60°, and 90°, respectively. Dimensions of the parameters are shown in Table III.

1) The detection results of variety orientation cracks: The temperature distribution of 45# steel and 316# stainless steel with different orientation cracks are presented in Fig. 11. It shows that there exists high thermal contrast (TC) around the cracks. In addition, it can be noted that with the angle increasing, the temperature is more concentrated either in the region of the bottom or tips of the crack. The temperature field on the sample is dependent on the different disturbances of magnetic field and eddy current caused by different oriented cracks. As the degree of cracks increases, the turbulence to magnetic flux tends to be lighter, whereas the turbulence to eddy current tends to be more severe. Due to the relative permeability of both 316# stainless steel and the air is 1, the disturbance of magnetic field caused by different cracks is slight. Thus, the detection results of 316# stainless steel mainly depend on the disturbance of eddy current. Consequently, different orientation cracks of 45# steel and all the nonparallel cracks of 316# stainless steel can be detected by the proposed structure.

TABLE III
DIMENSIONS OF THE POSITION PARAMETERS

Parameters	h1	h2	h3	L1	W1
Values(mm)	10	40	40	80	100

To estimate the ability and sensibility of the detection results, the TC is calculated. The calculation formula of TC is expressed as follows:

$$\mathrm{TC} = \frac{T_D - T_N}{T_N - T_0} \tag{21}$$

where T_D is the temperature in the defective region, T_N is the temperature in the nondefective region in the ROI, and T_0 is the initial temperature, which is 293.15 K.

The TC values of the detection results of different angles are presented in Table IV.

2) The detection results of different lift-off distances: To verify the influence of lift-off variations of the defect detection, both ferromagnetic and nonferromagnetic samples are employed for test. The lift-off distances are varied ranging from 0 to 15 mm with a step of 5 mm.

The TC and absolute temperature rise (ΔT) of the detection results under different lift-off distances are presented in Table V. As can be seen from the quantitative results, the small cracks in both 45# steel and 316# stainless steel have high TC values. It can be noted that the variances of the temperature amplitude are big, whereas the TC maintains at a high level when the lift-off varies.

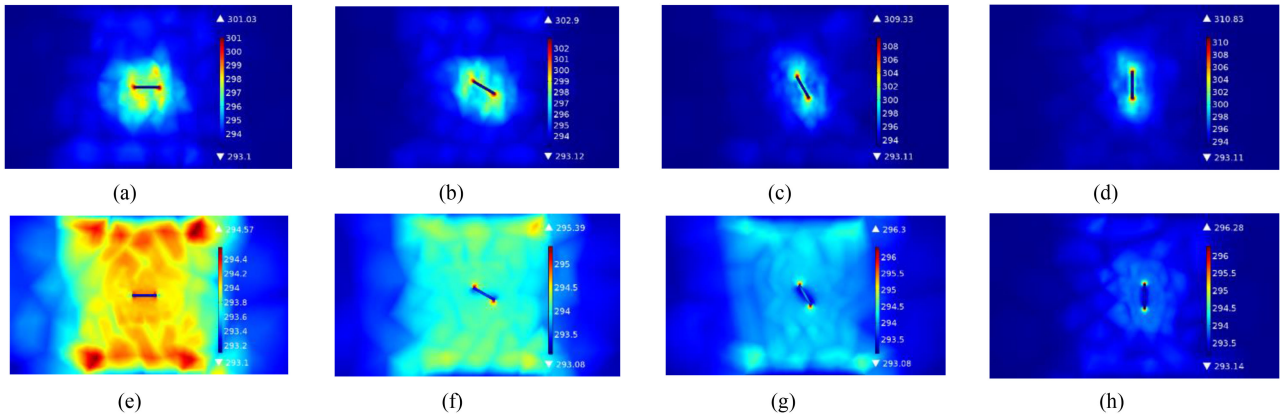

Fig. 11. Detection results of different orientations of 45# steel and 316# stainless steel. (a) 45# steel 0°. (b) 45# steel 30°. (c) 45# steel 60°. (d) 45# steel 90°. (e) 316# stainless steel 0°. (f) 316# stainless steel 30°. (g) 316# stainless steel 60°. (h) 316# stainless steel 90°.

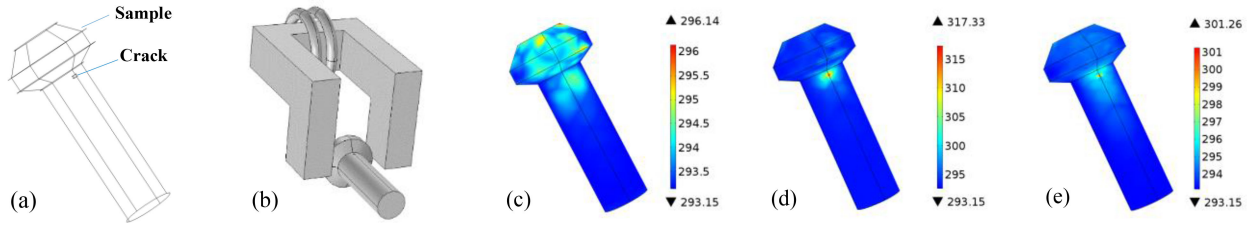

Fig. 12. Detection model of the sample with complex geometry and the results. (a) Sample and the crack. (b)Three-dimensional model of detecting. (c)–(e) Temperature distribution on steel without crack, 45# steel with a crack, and 316# stainless steel with a crack.

This indicate that the proposed model has good robustness to lift-off changes for defect detection.

3) Detection of Complex Geometry: The sample with complex geometry and the detection results are shown in Fig. 12. The position of the crack is close to the junction of two cylinders at different radii. In addition, the shape of the crack is a small cylinder, the radius and the height of which is both 0.5 mm. The three-dimensional model for detecting the sample with complex geometry is illustrated in Fig. 12(b).

Fig. 12(c)–(e) indicates the temperature distribution on the surface of the sample with a complex geometry. Fig. 12(c) shows the result of defect-free surface. It can be seen that the temperature at the edge is higher than the other part of the sample. Fig. 12(d) and (e) shows the results of defective surface of 45# steel and 316# stainless steel, respectively. With the high TC, the performance of the detection using the proposed excitation configuration is validated. The TC values of the detection results of complex geometry are presented in Table VI.

B. Experimental Validation

In order to validate the proposed model, experiments are implemented. The configuration system is shown in Fig. 13. The high-frequency power generator, Easyheat 224, is applied for excitation. The FLIR infrared camera with 0.08 k of temperature resolution and 200 Hz of maximum frame rate is used for recording. The new excitation coil with magnetic core whose inductance is 1uH is conducted. In the experiments, the frequency of the excitation current is fixed at 200 kHz. The current is adjusted with 350 A to provide sufficient energy, and the heating time is 200 ms. Experimental studies have been

TABLE IV
TC VALUES UNDER DIFFERENT ANGLES

	0°	30°	60°	90°
45# steel	265%	529%	710%	780%
316# stainless steel	×	149%	270%	470%

TABLE V
TC AND ΔT VALUES UNDER DIFFERENT LIFT-OFF DISTANCES

		0mm	5mm	10mm	15mm
45#	ΔT (K)	17.72	11.70	6.11	2.60
	TC (%)	780%	760%	610%	440%
316#	ΔT (K)	3.14	1.70	0.75	0.38
	TC (%)	470%	325%	300%	320%

TABLE VI
TC OF THE DETECTION RESULTS OF COMPLEX GEOMETRY

	Non-defect	45# steel	316# stainless steel
TC	×	736%	349%

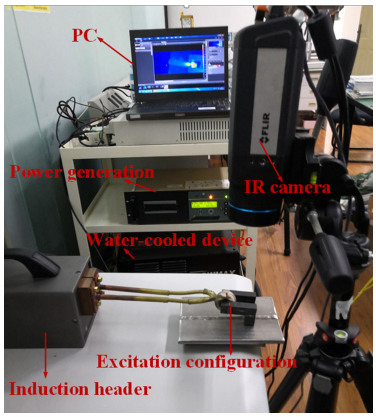

Fig. 13. Configuration of the ECPT experimental system.

conducted on natural fatigue cracks on several specimens under various surface conditions in order to validate the reliability and efficiency of the proposed excitation structure. In order to validate the performance of the proposed L-shaped electromagnetic thermography with conventional ECPT, controlled trials inducted by the line-coil ECPT system and the helix-coil ECPT system are employed for comparison.

1) Description of Samples: The screw sample with anomalistic shape is shown in Fig. 14(a), and the natural fatigue cracks are mainly concentrated at the root of the screw as marked by the red oval. Because the cracks are close to the edge or hide in the root, the diagnosis is inconvenient and difficult to be performed by using the conventional configuration of the ECPT system. The crack in the root of screw is shown in Fig. 14(b). From the figure, it can be seen that that the crack is extremely narrow and irregular.

The weld sample that belongs to a part of a pressure vessel is shown in Fig. 15(a). In order to validate the accuracy of detection, the penetration testing (PT) for the weld is conducted in advance, and the PT result is shown in Fig. 15(b). Note that the defect shown in the detection result by using PT is bigger than the real defect, and the natural crack in the weld is too small to be visualized. Fig. 15(c) is the 60 times magnified results of the crack, which is discontinuous and irregular in appearance. Consequently, the thermal pattern will be changed for the conductivity of the crack and is not absolutely zero. The rail specimen with RCF cracks is described in Fig. 16(a). In this experiment, the excitation structure is positioned normal to the specimen surface and close to the edge of the rail head, as shown in Fig. 16(b), where the RCF is known to be concentrated. The stainless steel sample from the nuclear industry is described in Fig. 17(a). The natural intergranular corrosion crack exists in the subsurface of the sample. The MT detection result is shown in Fig. 17(b). The defect is marked with the red rectangle.

Because the surface of the stainless steel is polished in the experiments and the crack is subsurface intergranular corrosion defect, black paint is used to cover the surface of stainless steel to deal with the high reflective surface and ensure the inspection effect [31]. For other metal samples, the emissivity of the material is maintained at a constant value. Thus, the IR camera corrects the temperature by setting different emittance for different materials.

In the comparative experiments, the radius and wire diameter of the helix coil with three turns are 22 and 6 mm, respectively. The wire diameter of the line coil is 6 mm. The excitation current for all comparison experiments is chosen as 350 A, 200 kHz. The relative position between samples and the inductors is shown in Fig. 18. The horizontal distance values m1, m2, m3, m4 are 3, 4, 5, and 5 mm, respectively. The lift-off distance between the coils and weld sample, stainless steel sample, rail sample, are 4, 6 and 5 mm, respectively. The screw sample is placed in the central axis of the helix coil.

A frame rate of 100 Hz for the FLIR infrared camera with a 640×240 array is used to detect the screw fatigue cracks and stainless steel intergranular corrosion defect, and a frame rate of 200 Hz for the FLIR infrared camera with a 640×120 array is used to detect the weld cracks and RCF cracks.

2) Results Analysis:

a) Detection results of screw fatigue crack: The verification experiments are performed by using the proposed excitation configuration model to detect the fatigue cracks in the root of screws, and the thermal images are captured by the infrared camera, as shown in Fig. 19(a) and (b). The results illustrate that the cracks are detected with high temperature contrast, and the crack shape is clearly presented. This indicates that the proposed excitation model can effectively detect natural microcracks in screws. Fig. 19(c) and (d) indicates that the cracks are submerged by the strong noise.

b) Detection results of weld crack: The experiment result of the weld crack by using the proposed model is shown in Fig. 20(a). The outline of the crack is clear, and the temperature distribution reflects that the cracks disturb the electromagnetic field. In comparison, Fig. 20(b) and (c) shows the detection result by using line coil and helix coil, respectively. As can be seen from Fig. 20(b), there is a lot of noise around the crack, and it is hard to be detected. In Fig. 20(c), part of crack 1 and crack 2 can be seen. However, the noise signal below the coil is very strong. Thus, the proposed structure has the advantage of detecting the rough surface because the electromagnetic fields were evenly distributed in the ROI.

c) Detection results of RCF cracks: Fig. 21 shows the detection result of RCF cracks, and the result discloses the presence of cracks at the edge of the rail head. The presence of the cracks in the ROI is clearly presented through the higher temperature contrast at the crack edges. This shows the effectiveness of the proposed excitation model in detecting the presence of multiple defects.

d) Detection results of subsurface intergranular corrosion defect: Fig. 22 shows the detection results of the subsurface intergranular corrosion defect in stainless steel plate. It can be seen from Fig. 22(a) that the thermal distribution pattern is intermittent at high temperature point, which is a typical form of natural crack caused by corrosion. From the detection result, it can be confirmed that the proposed-model-based ECPT system has reliable ability to accurately detect the subsurface narrow crack in stainless steel plate. In order to quantitative evaluate the detection ability of the proposed structure, the SNR of the

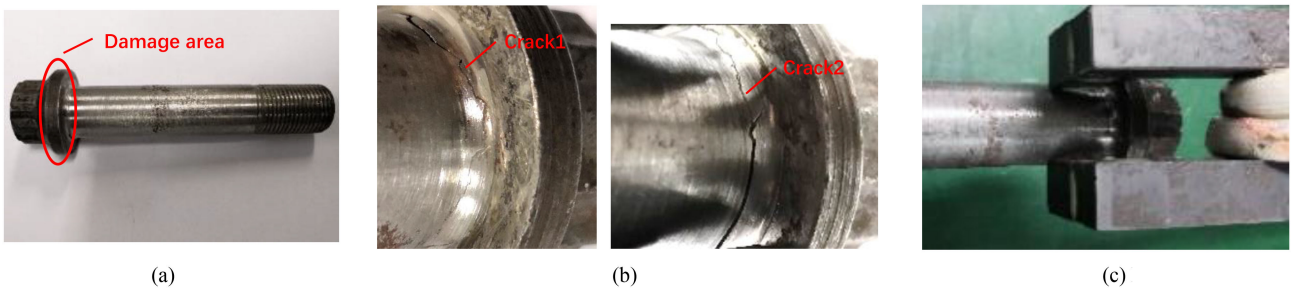

Fig. 14. Crack in the root of screw. (a) Screw and the damage area. (b) Cracks in the root of screw. (c) Detection position.

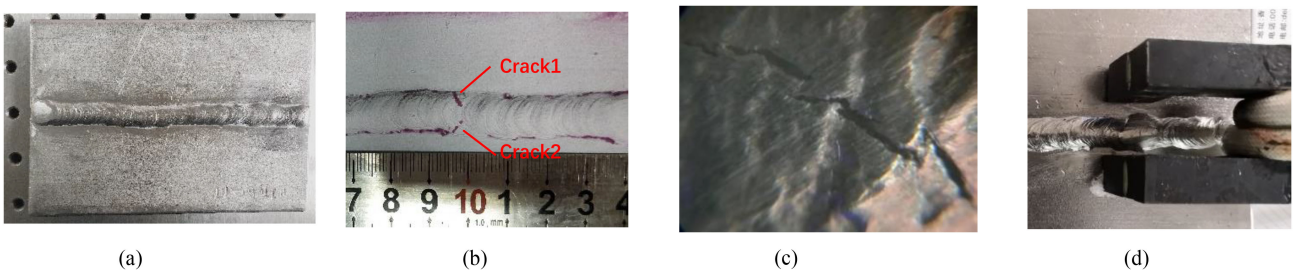

Fig. 15. Description of weld specimen and the surface natural cracks. (a) Picture of weld. (b) PT results of weld cracks. (c) Amplified result of crack1 (60×). (d) Detection position.

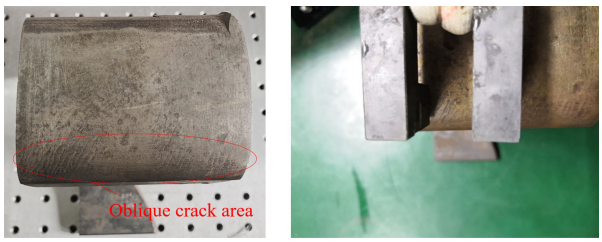

Fig. 16. Rail sample and the detection position. (a) Rail sample. (b) Detection position.

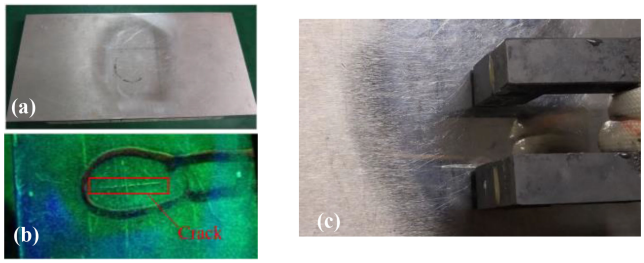

Fig. 17. Stainless steel sample and the subsurface natural crack. (a) Stainless steel sample. (b) MT result (c) Detection position.

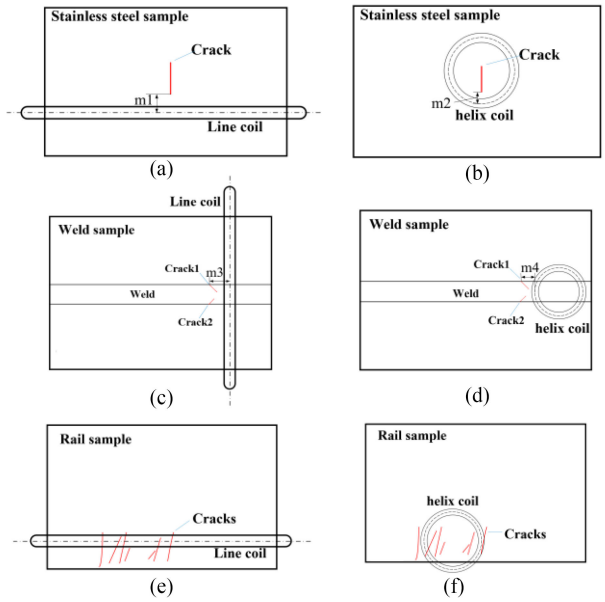

Fig. 18. Top view of detection models. (a) and (b) Stainless steel detection. (c) and (d) Weld detection. (e) and (f) Rail detection.

detection results by using three different excitation configurations is calculated. The calculation formula of SNR (dB) is the following:

$$\mathrm{SNR} = 20\log_{10}\left(\frac{T_{mD}}{T_{mN}}\right)[\mathrm{dB}] \tag{22}$$

where T_{mD} and T_{mN} are average temperature in defective and nondefective regions, respectively.

The quantitative analysis results of SNR are presented in Table VII. The "✗" refers to an occurrence in which the coil could not detect the microcrack in the corresponding experiment, the "–" refers to the coil is not applicable to that specimen. In the test of screws, the line coil cannot used to detect the cracks because

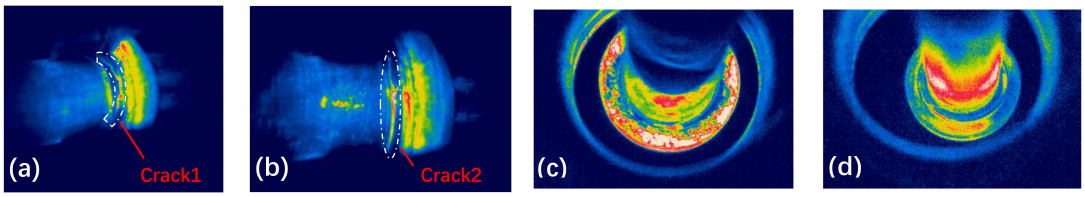

Fig. 19. Experiment results of screw using (a) and (b) proposed configuration and (c) and (d) helix coil.

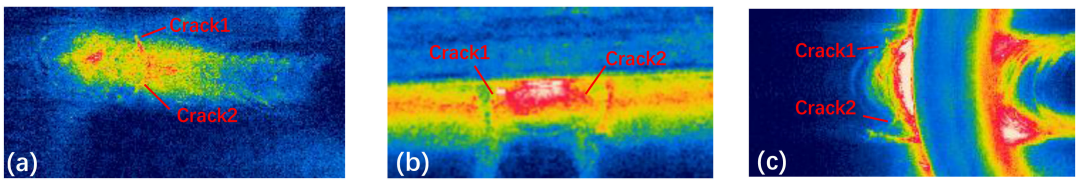

Fig. 20. Experiment results of weld cracks using (a) proposed configuration, (b) line coil, and (c) helix coil.

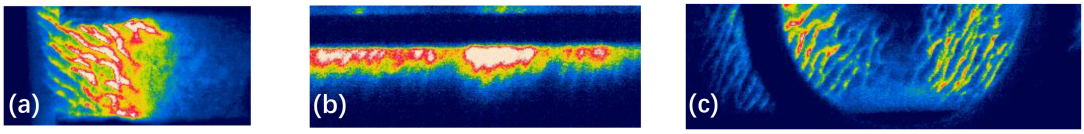

Fig. 21. Experiment results of RCFs using (a) proposed configuration, (b) line coil, and (c) helix coil.

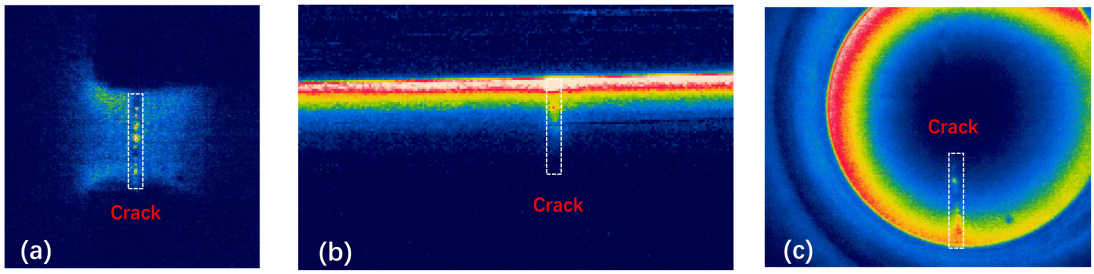

Fig. 22. Experimental results of the stainless steel plate using (a) proposed configuration, (b) line coil, and (c) helix coil.

TABLE VII
SNR (dB) OF DEFECT DETECTION EXPERIMENTS

	Screw1	Screw2	weld	RCFs	stainless steel
line-coil	--	--	0.358	2.628	0.608
helix-coil	×	×	×	5.846	2.029
proposed	7.203	12.256	2.032	8.810	15.874

of the complex geometry. As can be seen from the results, using the helix coil to detect the root of screws has an unsatisfactory performance, which still contains the complex background as well as noise interference. In contrast, the SNR of the proposed structure is equivalent to 12.256 and 7.203 dB, which indicates that the microcracks in the screws are successfully detected. In the experiments of the weld, the helix coil do not perform a good detection of the microfatigue crack, and the SNR of the proposed L-shaped structure improves by 1.674 dB compared with line coil. From results of RCFs, the SNR of the proposed structure is equal to 8.810 dB. Compared with line coil and helix coil, the SNR is enhanced with 6.182 and 2.964 dB, respectively.

In the test of stainless steel, the results obtained using the proposed structure have obvious superiority, and the SNR of the proposed structure leads to an improvement of 15.266 dB for line coil and 13.845 dB for helix coil. In general, compared with classical excitation sensing configurations, the proposed structure enhances the TC largely, and the energy can be excited effectively to strengthen the detectability of microcracks in complex geometry.

IV. Conclusion

In this article, an efficient excitation structure of the ECPT system was proposed. The theoretical derivative model of the excitation structure was developed. The detection results of natural cracks on the surface of several metallic materials were investigated, and the following conclusions can be drawn.

1) The proposed detection model provides an ROI that has relatively uniform magnetic field for increasing the TC between the defective and nondefective areas.
2) The proposed structure is suitable for the detection of microcracks in specimens with various geometric structures, such as RCF cracks in rail track, fatigue cracks in screw, small cracks in weld, and intergranular corrosion cracks in stainless steel.
3) The obtained experimental results validate the effectiveness of the proposed model and indicate that the proposed structure provides a possibility to dramatically increase portability and efficiency for detecting in-service workpiece.

Future work will focus on the quantitative detection of the proposed structure for detecting defects in different conditions.

References

[1] K. Miya, "Recent advancement of electromagnetic nondestructive inspection technology in Japan," *IEEE Trans. Magn.*, vol. 38, no. 2, pp. 321–326, Mar. 2002.

[2] R. Yang and Y. He, "Optically and non-optically excited thermography for composites: A review." *Infrared Phys. Technol.*, vol. 75, pp. 26–50, 2016.

[3] O. Lucia, P. Maussion, E. J. Dede, and J. M. Burdío, "Induction heating technology and its applications: Past developments, current technology, and future challenges," *IEEE Trans. Ind. Electron.*, vol. 61, no. 5, pp. 2509–2520, May 2013.

[4] B. Gao, W. L. Woo, Y. He, and G. Y. Tian, "Unsupervised sparse pattern diagnostic of defects with inductive thermography imaging system," *IEEE Trans. Ind. Inform.*, vol. 12, no. 1, pp. 371–383, Feb. 2015.

[5] N. Kasai, A. Takada, K. Fukuoka, H. Aiyama, and M. Hashimoto, "Quantitative investigation of a standard test shim for magnetic particle testing," *NDT E Int.*, vol. 44, no. 5, pp. 421–426, 2011.

[6] K. Fukuoka, S. Noma, M. Kobayashi, T. Ozaki, and Y. Oikawa, "Consideration of multi-coil type magnetizer for detection of omnidirectional crack in magnetic particle testing," *Int. J. Appl. Electromagn. Mechanics*, vol. 52, no. 3, pp. 1–8, 2016.

[7] R. Clark, W. D. Dover, and L. J. Bond, "The effect of crack closure on the reliability of NDT predictions of crack size," *NDT Int.*, vol. 20, no. 5, pp. 269–275, 1987.

[8] Z. D. Wang, Y. Gu, and Y. S. Wang, "A review of three magnetic NDT technologies," *J. Magnetism Magn. Mater.*, vol. 324, no. 4, pp. 382–388, 2012.

[9] M. Morozov, G Y. Tian, and P. J. Withers, "Noncontact evaluation of the dependency of electrical conductivity on stress for various Al alloys as a function of plastic deformation and annealing," *J. Appl. Phys.*, vol. 108, no. 2, pp. 2211–8142, 2010.

[10] M. P. Papaelias, M. C. Lugg, and C. Roberts, and C. L. Davis, "High-speed inspection of rails using ACFM techniques," *NDT E Int.*, vol. 42, no. 4, pp. 328–335, 2009.

[11] H. Shaikh *et al.*, "Use of eddy current testing method in detection and evaluation of sensitisation and intergranular corrosion in austenitic stainless steels," *Corrosion Sci.*, vol. 48, no. 6, pp. 1462–1482, 2006.

[12] O. Lucia, P. Maussion, E. J. Dede, and J. M. Burdio, "Introduction to the special section on induction heating systems," *IEEE Trans. Ind. Electron.*, vol. 61, no. 5, pp. 2504–2508, May 2014.

[13] B. Gao, P. Lu, W. L. Woo, G.Y. Tian, Y. Zhu, and M. Johnston, "Variational bayesian sub-group adaptive sparse component extraction for diagnostic imaging system," *IEEE Trans. Ind. Electron.*, vol. 65, no. 10, pp. 8142–8152, Oct. 2018.

[14] H. Zhang *et al.*, "Optical and mechanical excitation thermography for impact response in basalt-carbon hybrid fiber-reinforced composite laminates," *IEEE Trans. Ind. Inform.*, vol. 14, no. 2, pp. 514–522, Feb. 2018.

[15] Y. He and R. Yang, "Eddy current volume heating thermography and phase analysis for imaging characterization of interface delamination in CFRP," *IEEE Trans. Ind. Inform.*, vol. 11, no. 6, pp. 1287–1297, Dec. 2017.

[16] A. Yin, B. Gao, G. Y. Tian, W. L. Woo, and K. Li, "Physical interpretation and separation of eddy current pulsed thermography," *J. Appl. Phys.*, vol. 113, no. 6, 2013, Art. no. 064101.

[17] J. Zhao, B. Gao, W. L. Woo, F. Qiu, and G. Y. Tian, "Crack evaluation based on novel Circle-Ferrite induction thermography," *IEEE Sensors J.*, vol. 17, no. 17, pp. 5637–5645, Sep. 2017.

[18] Y. Wu *et al.*, "Weld crack detection based on region electromagnetic sensing thermography," *IEEE Sensors J.*, vol. 19, no. 2, pp. 751–762, Jan. 2019.

[19] N. Tsopelas and N. J. Siakavellas, "Performance of circular and square coils in electromagnetic–thermal non-destructive inspection," *NDT E Int.*, vol. 40, no. 1, pp. 12–28, 2007.

[20] M. He, L. Zhang, and W. Zheng, and Y. Feng, "Investigation on a new inducer of pulsed eddy current thermography," *AIP Adv.*, vol. 6, no. 9, 2016, Art. no. 095221.

[21] Y. Gao, Y. T. Gui, K. Li, J. Ji, P. Wang, and H. Wang, "Multiple cracks detection and visualization using magnetic flux leakage and eddy current pulsed thermography," *Sensors Actuators A, Phys.*, vol. 234, no. 6, pp. 269–281, 2015.

[22] M. Goldammer, H. Mooshofer, M. Rothenfusser, and J. Bass, J. Vrana, "Automated induction thermography of generator components," in *Proc. Rev. Prog. Quantitative Nondestruct. Eval.*, 2010, vol. 29, pp. 451–457.

[23] B. Gao, Y. He, W. Lok Woo, G. Y. Tian, J. Liu, and Y. Hu "Multidimensional tensor-based inductive thermography with multiple physical fields for offshore wind turbine gear inspection," *IEEE Trans. Ind. Electron.*, vol. 63, no. 10, pp. 6305–6315, Oct. 2016.

[24] B. Oswald-Tranta, "Thermo-inductive crack detection," *Nondestruct. Testing Commun.*, vol. 22, no. 2/3, p. 17, 2007.

[25] K. A. Hansen and E. C. Weisberg, "Asymmetric induction work coil for thermoplastic welding," U.S. Patent 5 444 220, 1995.

[26] J. Peng, G. Y. Tian, L. Wang, Y. Zhang, K. Li, and X. Gao, "Investigation into eddy current pulsed thermography for rolling contact fatigue detection and characterization," *NDT E Int.*, vol. 74, no. 6, pp. 72–80, 2015.

[27] R. Yang, Y. He, B. Gao, G. Y. Tian, and J. Peng, "Lateral heat conduction based eddy current thermography for detection of parallel cracks and rail tread oblique cracks," *Measurement*, vol. 66, no. 1/2, pp. 54–61, 2015.

[28] Y. He, Y T. Gui, and M. Pan, "An investigation into eddy current pulsed thermography for detection of corrosion blister," *Corrosion Sci.*, vol. 78, no. 1, pp. 1–6, 2014.

[29] Z Q. Zhu, Y. Pang, D. Howe, S. Iwasaki, R. Deodhar, and A. Pride, "Analysis of electromagnetic performance of flux-switching permanent-magnet machines by nonlinear adaptive lumped parameter magnetic circuit model," *IEEE Trans. Magn.*, vol. 41, no. 11, pp. 4277–4287, Nov. 2005.

[30] G. Temple, "Static and dynamic electricity," *Nature*, vol. 146, p. 446, 1940.

[31] I. Z. Abidin, G. Y. Tian, J. Wilson, S. Yang, and D. Almond "Quantitative evaluation of angular defects by pulsed eddy current thermography," *NDT E Int.*, vol. 43, no. 7, pp. 537–546, 2010.

Zewei Liu received the B.Sc. degree in automation from Henan Polytechnic University, Jiaozuo, China, in 2017. He is currently working toward the M.Sc. degree in nondestructive testing using induction thermography technique with the University of Electronic Science and Technology of China, Chengdu, China.

His research interests include automated eddy current thermography and fatigue damage testing and evaluation.

Bin Gao (M'12–SM'14) received the B.Sc. degree in communications and signal processing from Southwest Jiao Tong University, China, in 2005, the M.Sc. degree (with Distinction) in communications and signal processing and the Ph.D. degree in signal processing from Newcastle University, U.K., in 2011.

From 2011 to 2013, he was a Research Associate with Newcastle University, where he was involved with wearable acoustic sensor technology. He is currently a Professor of Nondestructive Testing, Sensors, Signal Processing and Machine Learning with the School of Automation Engineering, University of Electronic Science and Technology of China, Chengdu, China. He is also a very active reviewer for many international journals and long standing conferences. He has coordinated several research projects from the National Natural Science Foundation of China. His research interests include electromagnetic and thermography sensing, machine learning, and nondestructive testing and evaluation.

Gui Yun Tian (M'01–SM'03) received the B.Sc. degree in metrology and instrumentation and the M.Sc. degree in precision engineering from the University of Sichuan, Chengdu, China, in 1985 and 1988, respectively, and the Ph.D. degree in nondestructive testing, signal processing from the University of Derby, Derby, U.K., in 1998.

From 2000 to 2006, he was a Lecturer, a Senior Lecturer, a Reader, a Professor, and the Head of the Group of Systems Engineering, respectively, with the University of Huddersfield, U.K. Since 2007, he has been with Newcastle University, Newcastle upon Tyne, U.K., where he is currently a Chair Professor of Sensor Technologies. He is also an Adjunct Professor with the School of Automation Engineering, University of Electronic Science and Technology of China. He has coordinated several research projects from the Engineering and Physical Sciences Research Council, Royal Academy of Engineering, and FP7. Also, he has good collaboration with leading industrial companies, such as Airbus, Rolls Royce, BP, nPower, Networkrail, and TWI among others.